MASS RECOVERIES IN NANO TO MICROPARTICLE ANALYSIS OF ENVIRONMENTAL SAMPLES VIA FLOW FIELD FLOW FRACTIONATION-INDUCTIVELY-COUPLED PLASMA MASS SPECTROMETRY

by

Lucia Eliana Manangon

A thesis submitted to the faculty of
The University of Utah
in partial fulfillment of the requirements for the degree of

Master of Science

in

Geological Engineering

Department of Geology and Geophysics

The University of Utah

August 2013

Copyright © Lucia Eliana Manangon 2013

All Rights Reserved

The University of Utah Graduate School

STATEMENT OF THESIS APPROVAL

The thesis of **Lucia Eliana Manangon**

has been approved by the following supervisory committee members:

William P. Johnson	, Chair	**03/27/2013**
		Date Approved
Bruce K. Gale	, Member	**03/27/2013**
		Date Approved
Diego P. Fernandez	, Member	**03/27/2013**
		Date Approved

and by **D. Kip Solomon** , Chair of

the Department of **Geology and Geophysics**

and by Donna M. White, Interim Dean of The Graduate School.

ABSTRACT

In this study, mass loss mechanisms were examined during analysis of environmental samples by flow field flow fractionation (FlFFF) coupled to inductively-coupled plasma mass spectrometry (ICP-MS). Elemental compositions of particle size fractions across the range from 10 nm to <10 µm were determined. Mass losses from ICP-MS nebulization-ionization inefficiencies and particle sorption to the FlFFF membrane were shown to be significant for particle-associated elements. Mass loss from permeation through the FlFFF membrane was important for dissolved elements (K, Mg, Ca, and Sr) and partially dissolved elements (Mn, Cu, Pb, Mo, Ni, and Fe). Despite observed mass losses, at least 70% of all elemental masses were recovered, demonstrating that the detected particles were representative of the samples.

A mi madre, mi padre y hermano que son la fuerza para seguir caminando.

CONTENTS

LIST OF FIGURES

LIST OF TABLES

ACKNOWLEDGEMENTS

I am exceptionally thankful to William Johnson for giving me the opportunity to work with him and learn from his expertise. I really appreciate the invaluable help received from Diego Fernandez since the beginning of this project. I also want to thank Dr. Bruce Gale for his time and knowledge shared during our weekly meetings.

Thanks to all my family in Ecuador and Italy. They have motivated and supported me before and during this learning experience. Thanks to all my professors in Ecuador, especially to Ximena Diaz. My days in Salt Lake City would not have been enjoyable without the presence of my friends from Ecuador, Colombia, Peru, Brazil, and Argentina. Thank you for the support and fun times. Special thanks to Camilo for your help, time, and knowledge shared in the last part of this work.

This study was supported by a grant from the National Science Foundation's (NSF) Chemical, Biological and Environmental Transport program (Grant No. 0967037). Any opinions, findings, conclusions, or recommendations expressed in this material are those of the authors and do not necessarily reflect the views of NSF.

CHAPTER 1

INTRODUCTION

Nanoparticles (NP) of both engineered and natural origins tend to be size-distributed mixtures in aquatic matrices [1-7]. Since NP bioavailability and transport are mediated by NP size [3-7], determination of NP size distributions in aquatic media is critical to understanding their bioavailability and transport in aquatic settings.

Field flow fractionation (FFF) is an important method for determining size distributions of NP suspensions [8-11]. FFF is a group of techniques used to fractionate polydisperse NPs according to attributes such as size, density, and electrophoretic mobility. Fractionation occurs in a thin flat channel under laminar flow, wherein a perpendicular field is applied to separate particles according to the above characteristics [12]. Under the influence of the perpendicular field, the particles occupy different positions relative to the channel wall, experience different fluid velocities, within the channel depth (parabolic flow profile), and thereby elute at different times. The most commonly applied perpendicular fields are flow, sedimentation, and gravitational, corresponding to flow FFF (FlFFF), sedimentation FFF (SdFFF), and gravitational FFF (GrFFF).

In FlFFF, the perpendicular flow (cross-flow) can fractionate particles ranging in size from 1 nm to 100 μm [9]. This can be achieved by using two modes: normal mode (1 nm to ~1 μm) and steric mode (> ~1 μm). In normal mode, separation occurs due to

differential diffusion of different-sized particles against the cross-flow. In steric mode, the cross-flow drives all particles proximal to the bounding membrane, and separation occurs due to differential fluid drag and shear for different-sized particles.

FlFFF has been coupled to mass spectrometry and other detectors to determine elemental makeup of NPs as a function of size, as applied to engineered NPs [13-21] and environmental and biological samples [1, 22-27]. Relatively few studies have assessed sample mass recovery during FFF analysis, leading to concern regarding the representativeness of the results for the overall sample. Multiple mechanisms of mass loss may occur during FlFFF-ICP-MS, including: a) inefficiency of nebulization of the aqueous sample prior to introduction to the plasma [28, 29]; b) inefficiency of ionization in the plasma (e.g., incomplete destruction of particles [28, 29], or influence of other molecules/elements in the FlFFF carrier [30]); and c) sorption to, or permeation through, the bounding FlFFF membrane [31].

The above mass loss mechanisms have mostly been studied for engineered NPs. Combined nebulization-ionization inefficiencies were examined for engineered Au NPs by comparison of aqua regia-digested and nondigested samples [15, 20]. Negligible nebulization-ionization inefficiencies were observed by Schmidt, et al. [15], and inefficiencies ranging from 0 to 25% were observed by Hagendorfer, et al. [20], for various sizes and concentrations of Au NPs. While other studies added acid on-line prior to the ICP-MS detector, they did not quantify mass recovery [14, 32].

Mass losses due to sorption to, and permeation through, FlFFF membranes were examined for Ag NPs [14, 19], Au NPs [15], TiO_2 NPs [32], and polystyrene (PS) NPs [17] by comparison of fractionated and nonfractionated samples (with and without cross-

flow, respectively). Specifically, Poda, et al. [14] and Nischwitz, et al. [32] showed that mass losses due to membrane sorption/permeation ranged from 2-12% for Ag NPs (6.7-200 ppb), and 6-45% for TiO_2 NPs (34.7-195.8 ppm) extracted from sunscreens, respectively. However, as stated above, nebulization-ionization inefficiencies were assumed zero due to in-line acid addition prior to ICP-MS detection in both studies. Ulrich, et al. [19] showed greatly reduced peak areas in fractograms due to membrane sorption of Ag NPs (0.2-20 ppm) via UV detection, but did not provide mass recoveries. Schmidt, et al. [15] showed 5-50% sorption to the membrane of Au NPs (0.15-1.66 ppm), and accounted for ICP-MS ionization-nebulization inefficiencies, as described above. Schachermeyer, et al. [17] demonstrated (with detection via UV and multi-angle laser light scattering) sorption of 0-75% PS NP mass that depended on carrier composition.

Mass loss analysis is more complex for NPs in environmental samples due to their relatively low concentrations (often parts per trillion) in natural media, and the presence of various elements in solution causing variation in the ICP-MS signal (matrix effects). Many studies have examined NPs in natural media [1, 2, 22, 24-28, 31, 33-35], with many using detection via ICP-MS [26, 27, 33]. However, only one study examined mass loss via nebulization-ionization inefficiency [28], finding mass losses of 80% via nebulization-ionization inefficiencies for > 1 µm particles. Sorption to and permeation through the FlFFF membrane of environmental NPs were considered by three studies [26, 31, 35]. Neubauer, et al. [26] examined natural NPs from peat bog drainage and soil leachates, and found mass losses ranged from 9-55%. Dubascoux, et al. [31] characterized NPs in soil leachate, and reported mass losses approaching 40%. Plathe, et al. [35] examined riverbed sediment centrifugate (< 200 nm) and found mass losses

ranged from 25-43%. The above indicates quantification of mass losses in environmental sample analysis using FlFFF-ICP-MS still remains unclear and raises the concern of representative results.

In the present study, mass losses during FlFFF-ICP-MS were examined for two environmental samples: 1) effluent from a wastewater treatment plant; and 2) an anoxic, organic-rich, hypersaline brine from the Great Salt Lake. These samples were fractionated across the size range from 10 nm to 11 μm. Mass losses were distinguished between nebulization-ionization inefficiency and sorption to/permeation through the FlFFF membrane. Additionally, for the deep brine layer sample, sorption to and permeation through the FlFFF membrane were distinguished via analysis of the waste stream downstream of the membrane. The results were used to evaluate the representativeness of the measured elemental signals from particles in these environmental samples.

CHAPTER 2

FIELD FLOW FRACTIONATION THEORY

Field flow fractionation is a powerful and versatile separation technique applied in the characterization of various samples, such as macromolecules and particulate materials. Fractionation occurs in a ribbonlike channel under laminar flow, wherein a perpendicular field is applied to separate particles according to attributes such as size, density, and electrophoretic mobility [8, 12]. The applied field can vary depending on each subtechnique. The most common subtechniques are: flow FFF (FlFFF), sedimentation FFF (SdFFF), and gravitational FFF (GrFFF).

FFF theory explains how the applied field achieves separation of particles due to their different positions relative to the accumulation wall and different velocities. Under laminar regime, the fluid velocity at the surface of the channel walls is zero and maximum at the center of the channel. The applied field drives the particles toward the accumulation wall and locates them at different positions. The particles at different positions experience different velocities of the parabolic profile and exit the channel at different elution times [12]. The retention time t_r is determined using equation (1) [12, 36, 37]:

$$L - x' = \int_{t=0}^{t=t_r} u_z(x,t)dt \quad (1)$$

where L is the total length of the channel, x' is the length of the focusing point (Figure 1), and u_z is the average velocity of the analyte zone (particle cloud).

$$u_z(x,t) = \frac{\int_0^w v(x,y,t)\, c(y,t)\, dy}{\int_0^w c(y,t)\, dy} \tag{2}$$

In equation (2), w is the thickness of the channel, v is the fluid velocity, and c is the analyte concentration profile. The retention ratio R represents the retardation of the analyte zone relative to the average fluid velocity $\langle v \rangle$ due to the applied cross-flow field [12].

$$R = \frac{u_z(x,t)}{\langle v \rangle(x,t)} \tag{3}$$

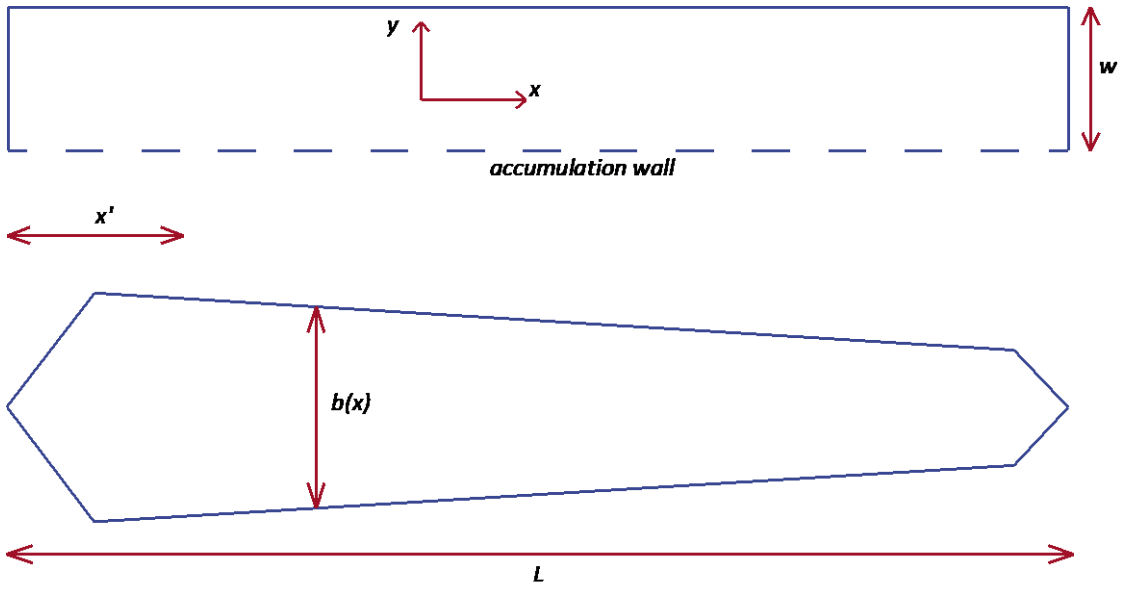

Figure 1 Trapezoidal asymmetrical FlFFF channel (side and front view)

The average fluid velocity $\langle v \rangle$ is determined according to the following equation:

$$\langle v \rangle(x,t) = \frac{\int_0^w v(x,y,t)dy}{\int_0^w dy} \tag{4}$$

Substituting equations (2) and (4) in equation (3):

$$R = \frac{w \int_0^w v(x,y,t)\, c(y,t)\, dy}{\int_0^w c(y,t)\, dy \int_0^w v(x,y,t)dy} \tag{5}$$

Under laminar regime [12, 36, 37]:

$$v(x,y,t) = 6\, \langle v \rangle(x,t) \left(\frac{y}{w} - \frac{y^2}{w^2}\right) \tag{6}$$

therefore

$$R = \frac{6 \int_r^w \left(\frac{y}{w} - \frac{y^2}{w^2}\right) c(y,t)\, dy}{\int_r^w c(y,t)\, dy} \tag{7}$$

The average fluid velocity $\langle v \rangle$ in a trapezoidal channel can be obtained by the following mass balance equation [36, 38, 39]:

$$\langle v \rangle(x,t) = \frac{Q_{out} + Q_c(t) - Q_c(t)\left(\frac{A(x)}{A_{tot}}\right)}{wb(x)} \tag{8}$$

where Q_{out} is the flow exiting the channel, Q_c is the time-dependent cross-flow, A is the accumulation wall area for position x, A_{tot} is the total accumulation wall area, and b is the channel breadth at position x. Equation (1) can be solved using equations (7) and (8) for the corresponding concentration profile.

The concentration profile can be obtained by solving the convection-diffusion equation [36, 40]:

$$\frac{dc}{dt} = -v_y(t)\frac{dc}{dy} + D\frac{d^2c}{dy^2} \tag{9}$$

where v_y is the time-dependent cross-flow velocity and D is the diffusion coefficient. When the cross-flow is constant, equation (9) is simplified to [12]:

$$v_y c(y) = D\frac{dc(y)}{dy} \tag{10}$$

Integrating equation (10) [12]:

$$c(y) = c_o\, e^{-\left(\frac{y\, v_y}{D}\right)} \tag{11}$$

v_y can also be expressed as the force of the applied field F on the particle divided by the friction coefficient f.

$$v_y = \frac{F}{f} \tag{12}$$

From the Nernst-Einstein equation:

$$f = \frac{kT}{D} \tag{13}$$

Substituting equations (12) and (13) in equation (11):

$$c(y) = c_o \, e^{-\left(\frac{yF}{kT}\right)} \tag{14}$$

The ratio between the thermal energy kT and the force F on a particle is called the mean layer thickness l, and it is the distance from the accumulation wall to the center of gravity of the analyte zone. l is generally expressed in the nondimensional form λ , known as the retention parameter [12].

$$\lambda = \frac{l}{w} \tag{15}$$

where w is the channel thickness. Substituting l in equation (15):

$$\lambda = \frac{kT}{Fw} \tag{16}$$

The analyte moves toward the accumulation wall at the velocity v_y determined by the cross-flow rate Q_C according to the following equation:

$$v_y = \frac{Q_C}{A_{tot}} \tag{17}$$

From equation (12):

$$F = v_y\, f \tag{18}$$

Substituting v_y in equation (18):

$$F = \frac{Q_C}{A_{tot}}\, f \tag{19}$$

Substituting F in equation (16):

$$\lambda = \frac{kT}{\left(\frac{Q_C}{A_{tot}} f\right) w} \tag{20}$$

From Stoke's law, the friction coefficient f is $6\pi\eta r$, where η is the dynamic viscosity of the fluid and r is the hydrodynamic radius of the particle. Substituting the coefficient f in equation (20):

$$\lambda = \frac{kT\, A_{tot}}{6\pi\eta\, Q_C\, w\, r} \tag{21}$$

λ can be related to the experimental retention ratio R, which in equilibrium is [36]:

$$R(\lambda) = \frac{1}{t_r}\left(\frac{w\,A_{tot}}{Q_C}\right) ln\left[1 + \frac{Q_C}{Q_{out}}\left(1 + \frac{A_{x\prime}}{A_{tot}}\right)\right] \quad (22)$$

where $A_{x'}$ is the accumulation wall area for the focusing point *x'*. R is related to λ according to the following equation [12]:

$$R = 6\lambda\, coth\left(\frac{1}{2\lambda}\right) - 12\lambda^2 \quad (23)$$

For asymmetrical channels with constant cross-flow, the hydrodynamic radius can be estimated by solving equation (22) for a determined retention time and equation (23) for the corresponding retention ratio *R*.

Commonly, programmed cross-flow is used to improve resolution in broad mixtures [12, 41-43]. When cross-flow decreases with time, the concentration profile will not relax instantaneously, and time is required to respond to the variable field. For this case, the concentration profile can be described by numerically solving equation (9). An approximate solution for equation (9) was presented by Giddings [40] using non-equilibrium theory to estimate *R* when relaxation effects are present [36]:

$$R = R^*\left(1 + \frac{2\,D}{v_y(t)^2}\;\frac{1}{Q_c(t)}\;\frac{dQ_c(t)}{dt}\right) \quad (24)$$

where R^* is the retention ration under equilibrium conditions.

Although relaxation effects have been considered to estimate particle size from retention time, discrepancy between the standard size and the theoretical size has been

found [44, 45]. Magnusson, et al. [44] demonstrated deviations of up to 16% from the predicted theoretical size even after considering relaxation effects. Combined factors such as equilibrium assumption (instantaneous relaxation), particle-particle interactions, and particle-membrane interactions may be causing the deviation.

CHAPTER 3

MATERIALS AND METHODS

Sample types and preparation

Two environmental samples were analyzed in this study. One sample was collected from the deep brine layer (DBL) of the Great Salt Lake, Utah on October 20, 2011. The DBL is a hypersaline, anoxic, organic-rich layer in the deepest portion of the Great Salt Lake, as described in Diaz, et al. [1]. The other sample was from a wastewater treatment plant (WWTP) located in Central Davis County, Utah, and was collected on April 14, 2012.

Two size fractions were prepared from each sample. A size fraction < 1.2 µm was prepared using syringe filters (Whatman 13mm x 1.2 µm, glass fiber) precleaned using 3 mL HCl (2.4%, trace metal grade) followed by 9 mL of water (Milli-Q). Negligible contribution to elemental signal was confirmed by analyzing Milli-Q water passed through the precleaned filters. The < 20 µm size fraction was prepared by first removing >20 µm particles by settling from the top 3 cm for 90 minutes (DBL) or by syringe filters (Bonna-Agela 25mm x 20 µm, polypropylene). The 20-µm polypropylene filters were cleaned as described above for the 1.2 µm filters. Negligible contribution to elemental signal was confirmed by analyzing Milli-Q water passed through the precleaned polypropylene filters.

Fractionation

Fractionation was performed using an asymmetric flow field flow fractometer (AF4 AF2000 FOCUS, Postnova Analytics, Landsberg, Germany), with channel length of 27.5 cm and nominal channel thickness of 350 µm. Regenerated cellulose membranes (10 kDa) were used with Fl-70 carrier (0.1% and 300 ppm NaN_3).

Two modes of fractionation were used. Normal mode was used to fractionate <1.2 µm sample fractions. The standards used for normal mode size calibration included 10 nm and 40 nm Au nanoparticles (Nanocomposix, San Diego, CA), and 98 nm, 210 nm, and 500 nm carboxylate-modified polystyrene (CMPS) microspheres (Molecular Probes, Inc., Eugene, OR). Steric mode was used to fractionate <20 µm sample fractions. The standards used for size calibration were 1.1 µm, 2.0 µm, 4.4 µm, and 9.1 µm CMPS microspheres (Polysciences, Inc., Warrington, PA).

Both normal and steric modes involve sample injection-focus, elution, and rinsing steps. Each of these fractionation steps produce effluent streams (flows) going to: a) the detectors; b) to waste; and c) to "slot". The corresponding operating conditions are shown in Table 1.

Detection

Three detectors were used in series during normal mode fractionation: 1) UV (254 nm) (SPD-20A, Shimadzu, Kyoto, Japan); 2) multi-angle light scattering (MALS) (DAWN HELEOS-II, Wyatt Technology, Santa Barbara, CA) with 18 angles, as well as dynamic light scattering (DLS) detection (DynaPro NanoStar, Wyatt Technology, Santa Barbara, CA) on the 90° detector coupled; and 3) ICP-MS (7500 ce, Agilent

Table 1 AsFlFFF operating conditions for normal and steric modes for the WWTP effluent and DBL sample

NORMAL		*STERIC*	
INJECTION-FOCUS		**INJECTION-FOCUS**	
Detector flow (mL/min)	0.4	Detector flow (mL/min)	2.5
Slot flow (mL/min)	0.6	Slot flow (mL/min)	2.0
Injection flow (mL/min)	0.2	Injection flow (mL/min)	0.3
Injection time (min)	9	Injection time (min)	7
Cross-flow (mL/min)	0.7	Cross-flow (mL/min)	1.5
Transition time (min)	1	Transition time (min)	1

ELUTION			**ELUTION**		
Cross-flow (mL/min)	Time (min)	Type	Cross-flow (mL/min)	Time (min)	Type
0.7	13.5	Constant	1.5	3	Constant
0.5	1	Linear	1.5	15	Linear
0.27	26	Linear	-	-	-

RINSE		**RINSE**	
Tip flow mL/min	Time	Tip flow mL/min	Time
0.4	5	1	5

Technologies, Santa Clara, CA) with collision cell for kinetic discrimination (via He) of interferences. Elements measured were: Mg, Al, Si, K, Ca, P, Ti, Mn, Fe, Ni, Cu, Zn, Sr, Mo, Pb.

During steric mode fractionation, detectors were used in the same order; however, for elemental analysis (ICP-MS), discrete effluent fractions were collected due to the high channel flow rate during steric fractionation. An additional off-line detector was used to measure dissolved organic carbon (DOC) in the WWTP and the DBL (TOC-5000A, Shimadzu, Kyoto, Japan) for samples filtered through 0.45 µm syringe filters (Whatman 13 mm x 0.45 µm, glass fiber).

Experimental design

A mass balance was performed to evaluate mass loss mechanisms. Two different approaches were used to examine recoveries for the two different fractionation methods (two different size fractions) because of on-line versus off-line ICP-MS utilization (Figure 2).

Size fraction < 1.2 µm

Mass recovery for the < 1.2 µm fraction (normal mode fractionation) was performed as follows. The total elemental masses were determined in digested samples (digestion procedure shown in the Appendix) introduced off-line to the ICP-MS. The corresponding fractogram peak area was determined for a parallel digested sample introduced on-line (with carrier flow but without fractionation), referred to as "Total" (Figure 2), and representing the sample with no nebulization-ionization or membrane sorption/permeation losses.

To evaluate mass loss mechanisms due to: a) particle nebulization-ionization, and b) membrane sorption/permeation, two introduction methods were used for nondigested samples. To examine potential effects of particle nebulization-ionization, samples were injected into the FFF channel without cross-flow, referred to as "No-xflow" (Figure 2). To examine membrane sorption/permeation effects, samples were injected into the FFF channel with cross-flow, referred to as "Xflow-detector" (Figure 2). Cs (5 ppb) was added to the carrier solution as an internal standard to verify constancy of signal during fractionation for all measured elements despite pressure/flow changes associated with the fractionation protocol.

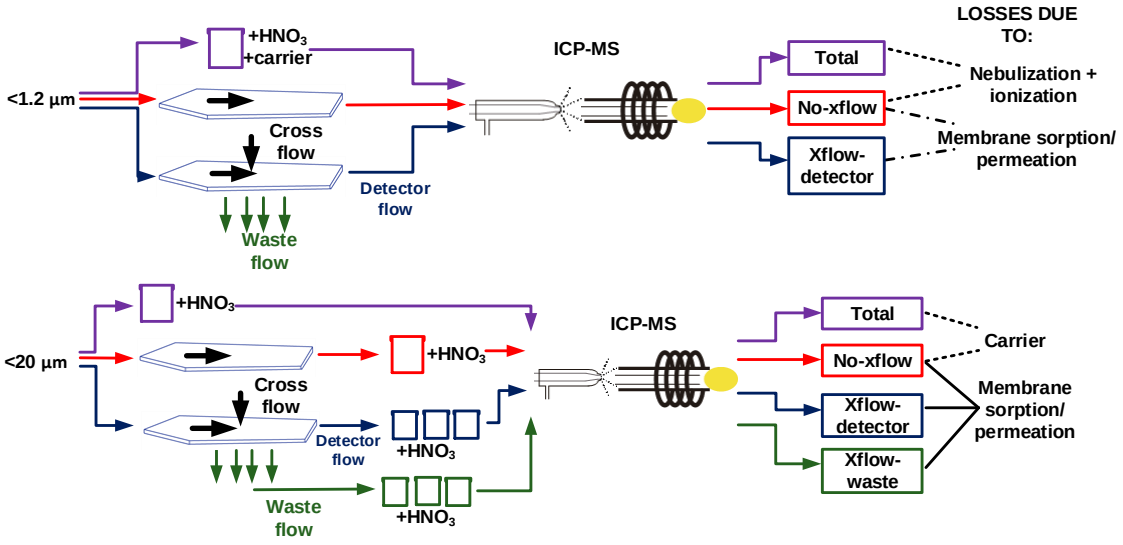

Figure 2 Schematic of methodology applied to <1.2 µm and <20 µm size fractions to determine mass loss mechanisms.

Size fraction < 20 µm

Mass recovery for the < 20 µm fraction (steric mode fractionation) was performed as follows. The elemental masses were determined in digested < 20 µm samples that were introduced off-line to the ICP-MS, and referred to as "Total" (Figure 2). In fact, all samples, even FlFFF fractionated samples, were introduced to the ICP-MS off-line, since steric mode fractionation involves flow rates too high for on-line ICP-MS analysis. Therefore, any nebulization-ionization inefficiencies in the steric mode (< 20 µm) analyses would not derive from particle influences, but could derive from the presence of organic and other molecules/elements in the FlFFF carrier. To examine carrier effects on nebulization-ionization efficiencies, samples were injected into the FlFFF channel without cross-flow, referred as "No-xflow", and were compared to "Total" (Figure 2). To examine membrane sorption/permeation effects, No-xflow samples were compared to X-flow samples. Furthermore, to distinguish membrane sorption from permeation in

samples with sufficiently high elemental concentrations, both the detector and waste streams were analyzed, and referred to as “Xflow-detector” and “Xflow-waste”, respectively (Figure 2).

CHAPTER 4

RESULTS AND DISCUSSION

Fractograms

Normal mode fractograms for standards were run three times to examine resolution and reproducibility. Resolved peaks were obtained for all five standards introduced as a mixture: 10 and 40 nm Au, 98, 210, and 500 nm CMPS (Figure 3). The method was reproducible despite changing the membranes between different standard and sample runs. The 10 nm Au nanoparticle was better detected by the UV detector (Figure 3), as expected, since light scattering intensity increases with particle size. The signal was low for the 500 nm CMPS due to a lower injected particle concentration (factor of 15) relative to the 210 nm CMPS concentration. Calibration equations from normal mode standards were obtained to convert elution time to size (see Appendix). Comparison between the standard size and the theoretical size was performed (see Appendix) using equations (22) and (23) explained in the FFF theory section.

Steric mode fractograms for standards were run twice to examine resolution and reproducibility (Figure 4). The peaks for the 1.1, 2.0, 4.4, and 9.1 μm CMPS were well resolved. The method was reproducible despite changing of membranes between runs. Higher signals were detected for the 9.1 and 4.4 μm CMPS microspheres in one of the replicates due to a higher particle concentration (factor of 3) relative to the other

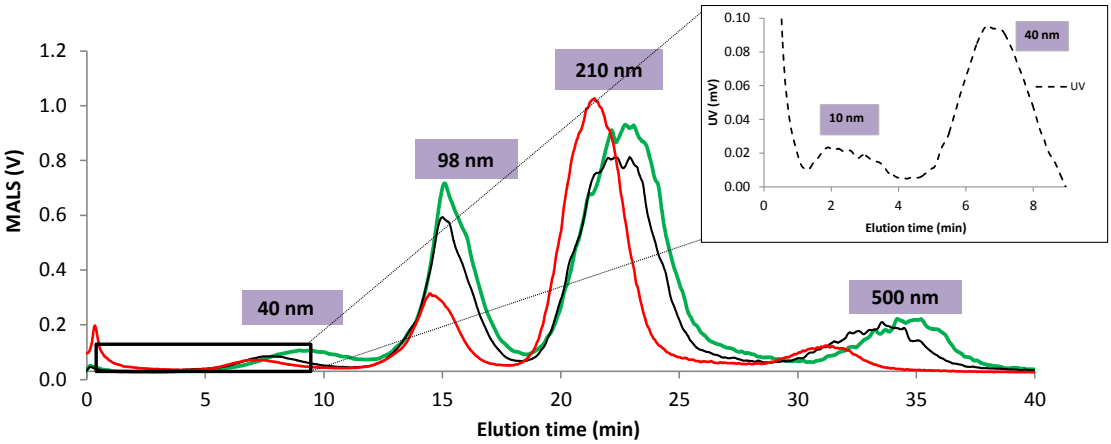

Figure 3 Fractograms of normal mode standards (10 nm Au, 40 nm Au, 98, 210, and 500 nm CMPS). Three replicates shown. MALS detection (solid lines), UV detection (inset, dashed line)

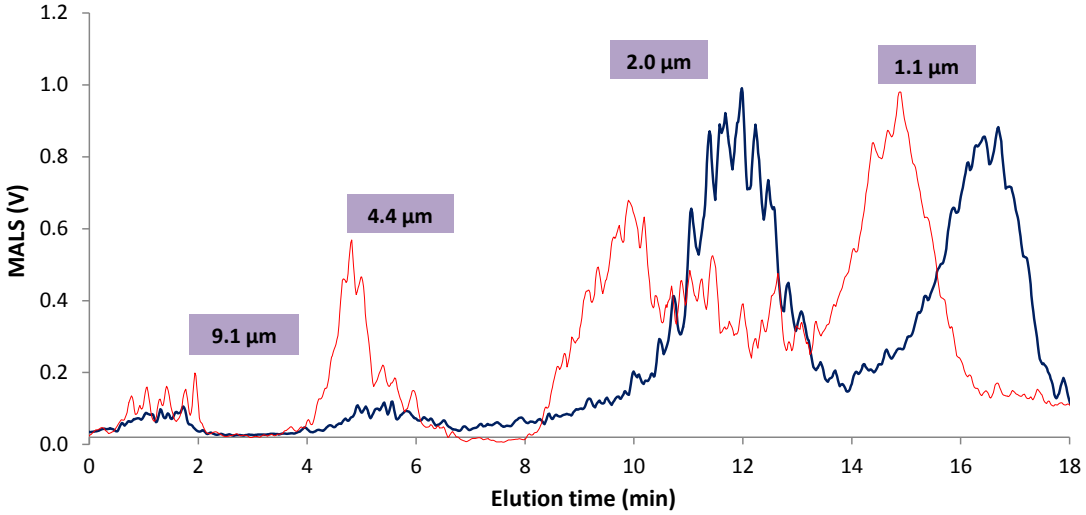

Figure 4 Fractograms of steric mode standards (mixture of 1.1, 2.0, 4.4, and 9.1 µm CMPS). Two replicates shown.

replicate. Calibration equations from steric mode standards were obtained to convert elution time to size (see Appendix).

WWTP sample

MALS and ICP-MS fractograms for the <1.2 µm (normal mode) fraction of the WWTP sample (Figure 5) showed peaks in the size range between 10 and 120 nm. The 45-75 nm MALS peak corresponded to ICP-MS detection of the elements K, Fe, and Ni. The 100-120 nm MALS peak corresponded to ICP-MS detection of P. In addition, a 10 – 30 nm peak for Fe, K, and Ni was detected using ICP-MS, but was not detected via MALS. DOC measurements on the <1.2 µm fraction of the WWTP sample yielded a value of 4 mg/L, suggesting that carbon may have been a significant constituent in the MALS peaks. The MALS fractogram for the <20 µm (steric mode) fraction of the WWTP sample showed negligible signal (see Appendix); whereas, the ICP-MS analysis of discrete size fractions are described in the Mass Recoveries section. Size information could not be extracted from the MALS signal due to lack of angular dependence of the signal (see Appendix).

DBL sample

MALS and ICP-MS fractograms for the <1.2 µm fraction (normal mode) of the DBL sample (Figure 6) showed peaks in the size range between 10 and 160 nm. The 10-30 nm MALS peak corresponded to ICP-MS detection of the elements Fe, Ni, Sr, and Mo.

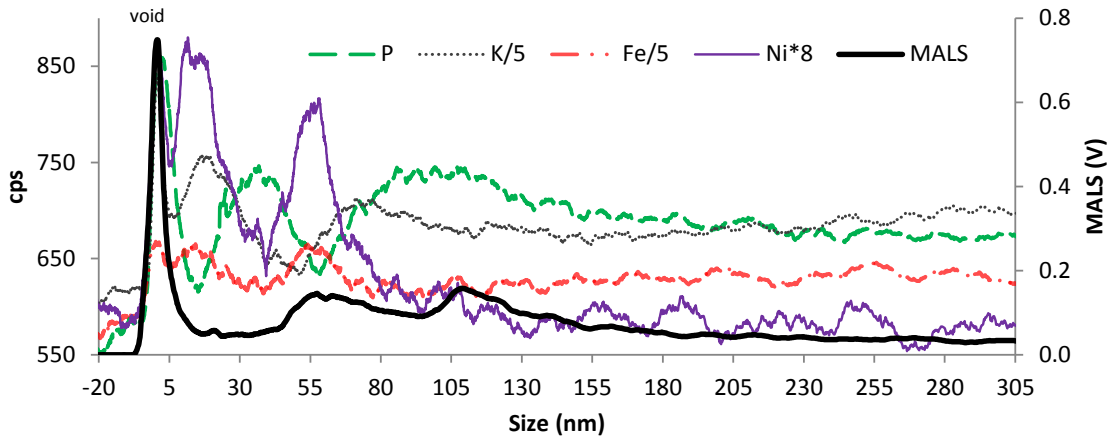

Figure 5 WWTP sample normal mode fractograms with detection via ICP-MS and MALS. Concentrations were divided (/) or multiplied (*) by specified factors to plot on one scale.

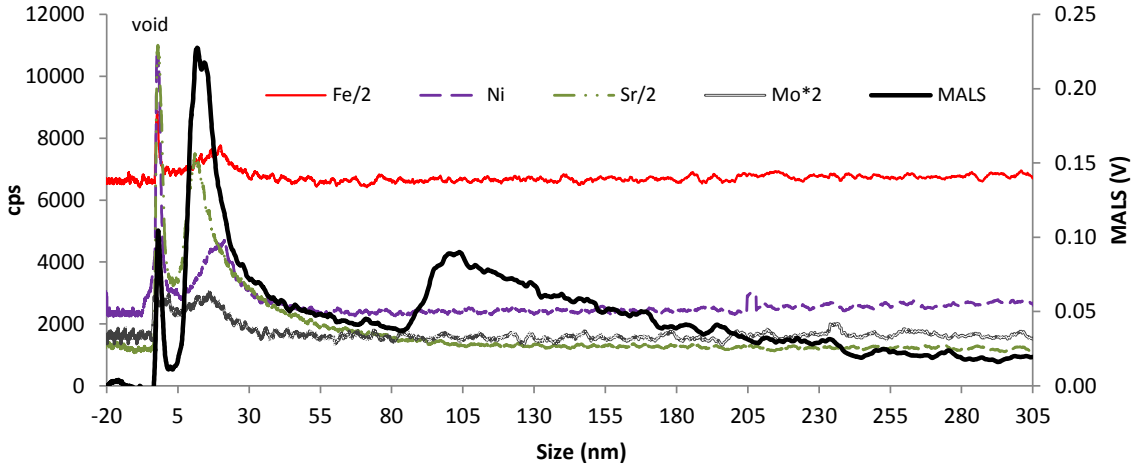

Figure 6 DBL normal mode fractograms with detection via ICP-MS and MALS. Concentrations were divided (/) or multiplied (*) by specified factors to plot on one scale.

The 90-160 nm MALS peak had no corresponding ICP-MS-detected elements. DOC measurements suggested that carbon was a significant constituent in the MALS peaks.

The <20 µm size fraction of the DBL sample (Figure 7) showed peaks in the size range from ~1 µm (steric transition) to ~11 µm. The 1-3 µm and 7 – 11 µm MALS peaks corresponded to ICP-MS-detection of the elements Fe, Sr, Mn, Ni, Pb, Mo, and Cu, as shown for discrete size fractions (Figure 7). Fe was the major constituent in all size fractions, and Cu was significant in all size fractions; whereas the other elements varied among the size fractions. The size fractions with the greatest combined elemental masses corresponded to largest MALS peaks, indicating qualitative correspondence between the two analyses. The degree to which the detected elements described above represent the overall samples warrants further consideration, as described below.

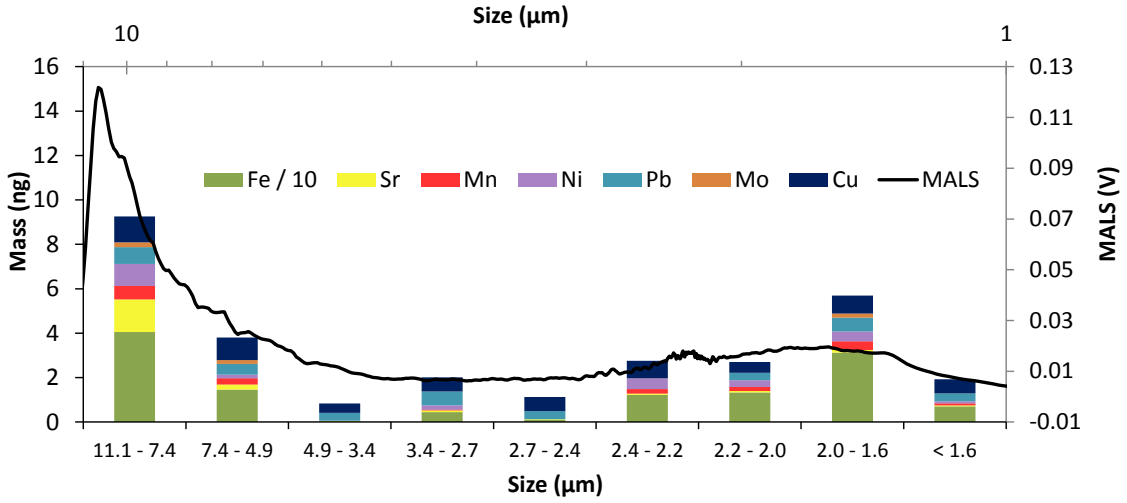

Figure 7 DBL steric mode fractogram (MALS) superimposed on discrete micro-particulate size fractions with detection via ICP-MS. Concentrations were divided (/) by specified factors to plot on one scale.

Mass recoveries

Elemental masses for the different introduction methods were compared to understand the extent and mechanisms of mass loss during analysis.

WWTP sample

Elemental masses in the < 20 µm fraction were similar to those in the < 1.2 µm fraction, demonstrating that none of the elements tested were associated with particles larger than 1.2 µm (Table 2 and Appendix). Concentrations corresponding to the masses in Table 2 are provided in the Appendix.

Particle nebulization-ionization inefficiencies (difference between Total and No-xflow masses) (Table 2) were significant for Fe, Ni, and Cu. Of these elements, Fe and

Table 2 Total elemental masses (µg) in the < 1.2 µm WWTP fraction and < 20 µm DBL fraction in the injection volume (300 µL)

	< 1.2 µm WWTP			**< 20 µm DBL**			
	Total	**FFF**		**Total**	**FFF**		
		No-xflow	**Xflow-detector**		**No-xflow**	**Xflow-detector**	**Xflow-waste**
Mg	9.559	10.68	-	1200	1664	<DL	1065
K	3.1855	3.27	0.108	900	1004	1	683
Ca	18.5047	20.48	-	68.4	71.4	<DL	44.3
Mn	0.0042	0.0039	-	0.029	0.034	0.002	0.009
Fe	0.0062	0.0012	0.0014	0.170	0.232	0.125	0.037
Ni	0.0007	0.0001	0.0001	0.005	0.008	0.003	0.002
Cu	0.0034	0.0024	-	0.03	0.073	0.007	0.032
Sr	0.0972	0.1062	-	0.774	0.851	0.002	0.614
Mo	0.0012	0.0012	-	0.009	0.010	0.001	0.005
Pb	-	-	-	0.00108	0.031	0.004	0.008

Ni were shown to exist as nanoparticles (Figure 5), suggesting that the presence of particles may decrease ICP-MS nebulization-ionization efficiency.

Mass loss from membrane sorption-permeation (difference between Xflow-detector and No-xflow masses) (Table 2) was significant for all the measured elements, except for Fe and Ni. It is likely that elements expected to have a significant dissolved fraction such as Mg, Ca, and Sr were lost due to membrane permeation; however, this expectation was not verified for the WWTP sample because concentrations were too low to allow detection in waste streams.

DBL sample

Total elemental masses in the DBL sample show that there was negligible mass in the < 1.2 µm fraction (see Appendix). In contrast, < 20 µm fraction masses were significant for Mg, K, Ca, Fe, Ni, Cu, Sr, and Pb (Table 2). The concentrations corresponding to the reported mass are shown in the Appendix.

Particle nebulization-ionization inefficiencies resulting from carrier effects (difference between Total and No-xflow masses) (Table 2) were not significant. In fact, Fe, Cu, and Pb recoveries increased slightly, possibly due to enhanced ionization in the presence of surfactant in the carrier (e.g. [30, 46]). In contrast to the negligible carrier effects, there were significant membrane sorption/permeation effects (Table 2), as shown by comparing Xflow-detector and Xflow-waste to No-xflow.

In the cases of Fe, Mn, Ni, Pb, Mo, and Cu, significant masses were detected in both the Xflow-detector and Xflow-waste streams, suggesting that these elements associated with both microparticle (not permeating the membrane), and dissolved

(permeating the membrane) phases. Notably, Fe, Ni, Mo, and Sr were also detected as nanoparticles in the normal-mode fractograms (Figure 6), suggesting that nanoparticles smaller than the steric transition (~1 μm) may have contributed to the steric mode signals. However, the mass detected in the <1.2 μm fraction normal-mode fractogram (nanoparticles) was negligible relative to that detected for the steric mode <20 μm fraction (microparticles) (see Appendix), indicating that the Fe, Ni, Sr, and Mo signals corresponded almost exclusively to microparticles.

Elements Mg, K, Ca, and Sr were detected predominantly in the xflow-waste stream, indicating that these elements had permeated the membrane and therefore were predominantly dissolved.

Implications

At least 70% of element mass present in the DBL and WWTP samples was recovered. The missing mass for each sample can be attributed to the following two influences: a) particle-driven nebulization-ionization inefficiencies, which were significant for Fe and Ni in the WWTP sample (Figure 8); b) membrane sorption-permeation losses, which were significant for P and K in the WWTP sample (Figure 8), and for Mg, K, Ca, Mn, Fe, Ni, Cu, Sr, Mo, and Pb in the DBL sample (Figure 9). Permeation through the membrane was demonstrated to be important for Mg, K, Ca, and Sr in the DBL sample due to their presence solely in the waste stream downstream of the FFF membrane. The presence of measurable Mn, Fe, Ni, Mo, and Pb in both the waste stream downstream of the FlFFF membrane and in the detector (DBL sample) suggests that mass loss for these elements occurred due to both sorption to, and permeation

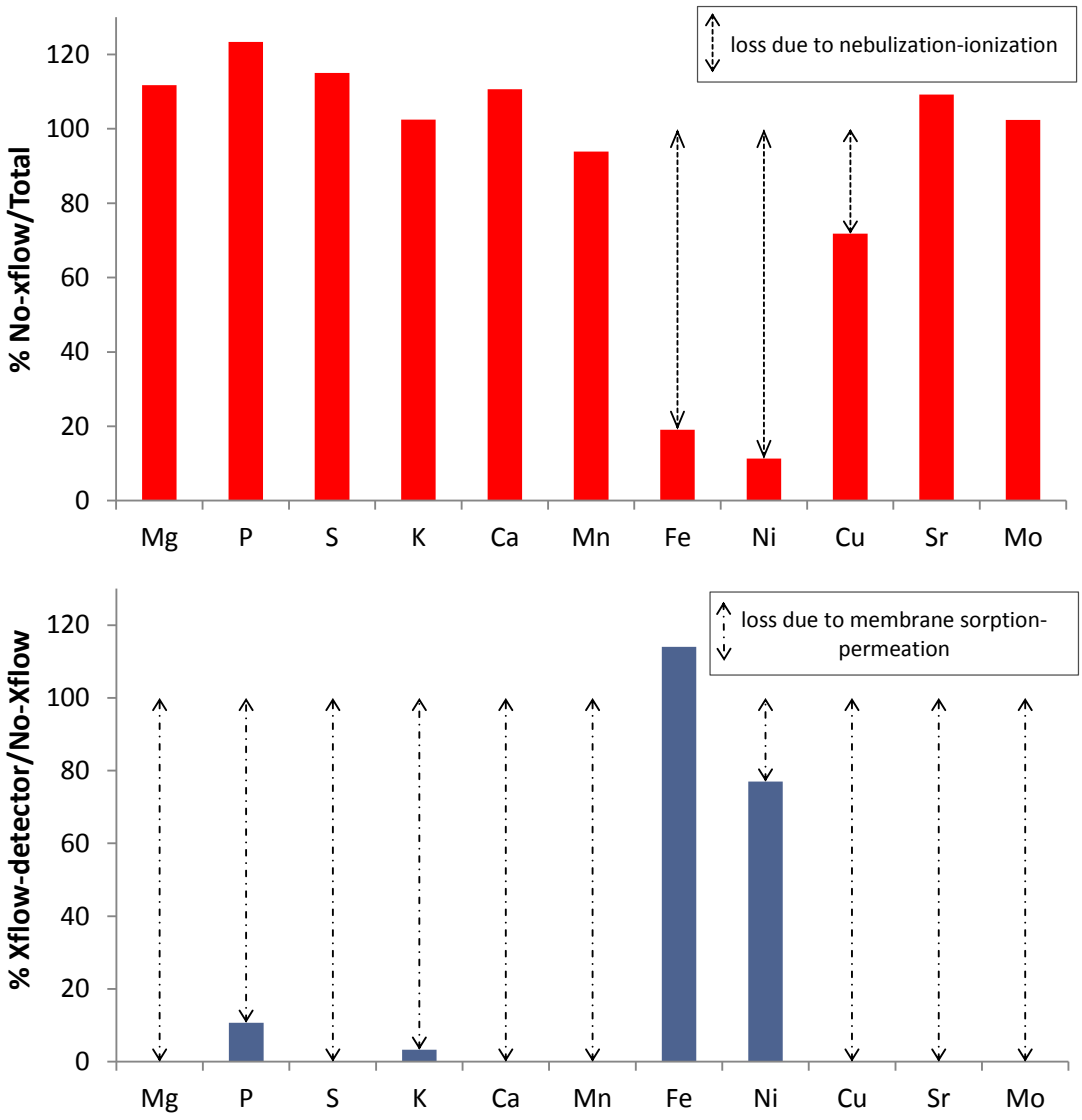

Figure 8 WWTP mass losses due to nebulization-ionization inefficiencies (above) and combined sorption to, permeation through, the membrane (below).

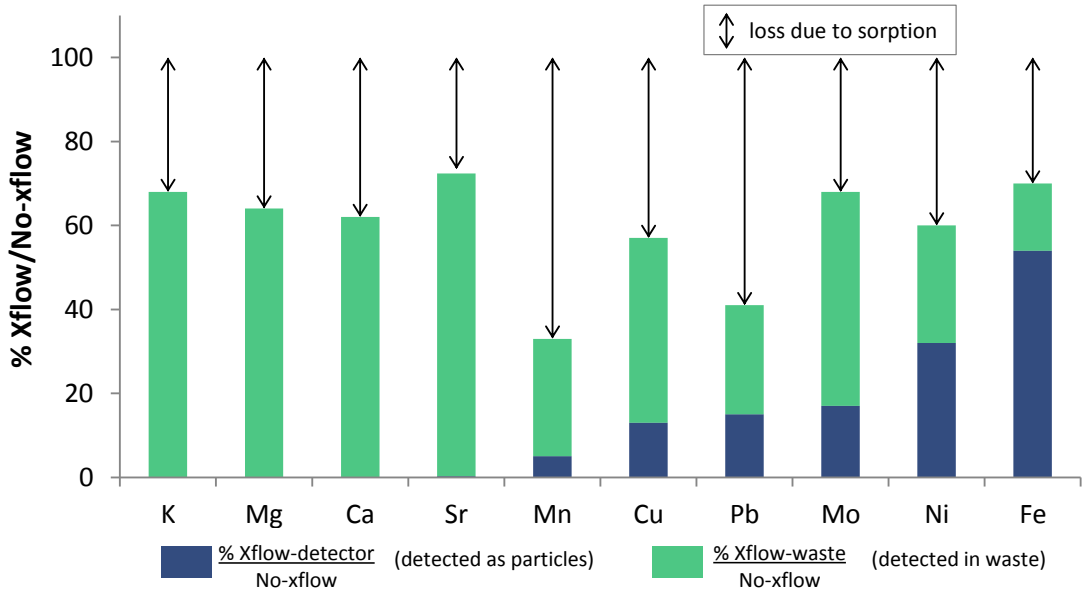

Figure 9 DBL mass losses due to nebulization-ionization inefficiencies, permeation through the membrane, and sorption to the membrane.

through, the membrane for the microparticulate and dissolved phases, respectively, of these elements.

Together, the results indicate that: i) For elements with major dissolved fractions, while there will be no particle-driven reduction of nebulization/ionization efficiencies, there will be mass loss via permeation through the FFF membrane; ii) For elements with significant particulate fractions, mass loss via both sorption to the FFF membrane and nebulizing/ionizing inefficiencies during ICP-MS may be significant; iii) The mass balance showed that the measured signal from the particulate elements was representative of the sample, despite the mass losses that were identified.

APPENDIX

SUPPORTING INFORMATION

Digestion Procedure

2 mL of each sample were poured in 7-mL teflon vials and weighed. 1mL of trace metal grade (TMG) HNO_3 was added. The mixture was evaporated in a hot plate for around 20 minutes. 1.5 mL of TMG HNO_3 and 0.5 mL of TMG HF were added and refluxed in a hot plate for 45 minutes. The mixture was evaporated for 30 minutes. 3 mL of 1% TMG HNO_3 were added. The final mixture in the vial was weighed.

Table A 1 Masses (µg) and concentrations (ppm) of elements in the < 20 µm fraction of the WWTP effluent

Element	**< 20 µm**	
	Mass in 300 µL of sample	**Concentration**
Mg	9.463	31.545
K	3.1980	10.660
Ca	18.4896	61.632
Mn	0.0044	0.015
Fe	0.0081	0.027
Ni	0.0006	0.002
Cu	0.0036	0.012
Sr	0.0975	0.325
Mo	0.0012	0.004

Table A 2 Concentrations (ppm) in the < 1.2 µm WWTP fraction and < 20 µm DBL fraction

Element	< 1.2 µm			< 20 µm			
	WWTP			DBL			
	Total	FFF		Total	FFF		
		No-Xflow	Xflow		No-flow	Xflow-detector	Xflow-waste
Mg	31.864	35.62	-	4000	5549	0.71	3550
K	10.618	10.88	0.36	3000	3349	3.50	2276
Ca	61.682	68.25	-	228	238	0.68	147
Mn	0.014	0.013	-	0.0972	0.112	0.006	0.030
Fe	0.021	0.004	0.005	0.52	0.774	0.415	0.123
Ni	0.002	0.0003	0.0003	0.018	0.028	0.009	0.067
Cu	0.012	0.008	-	0.10	0.243	0.022	2.047
Sr	0.324	0.35	-	2.58	2.84	0.007	0.017
Mo	0.004	0.004	-	0.030	0.033	0.002	0.030
Pb	-	-	-	0.0036	0.105	0.013	0.027

Table A 3 Masses (µg) and concentrations (ppm) of elements detected associated with nanoparticles in normal mode of the DBL

Element	< 1.2 µm	
	Mass in 300 µL of sample	Concentration
Fe	0.0050	0.0166
Ni	0.0003	0.0010
Mo	0.0001	0.0003
Sr	0.0004	0.0013

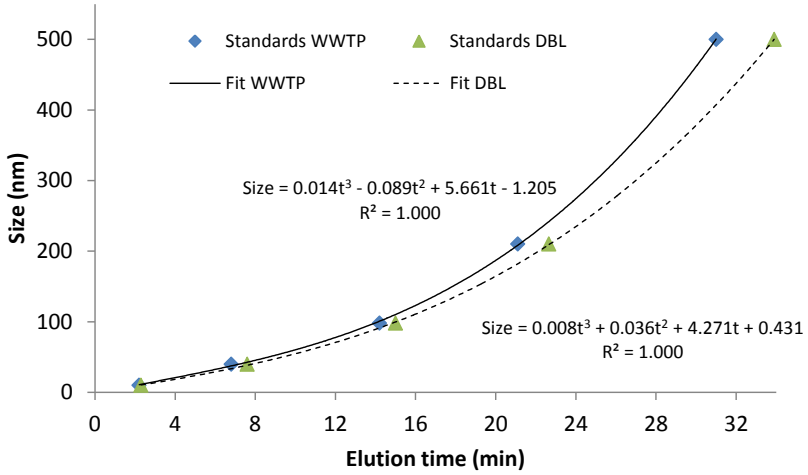

Figure A 1 Calibration equations for normal mode obtained from standard fractograms

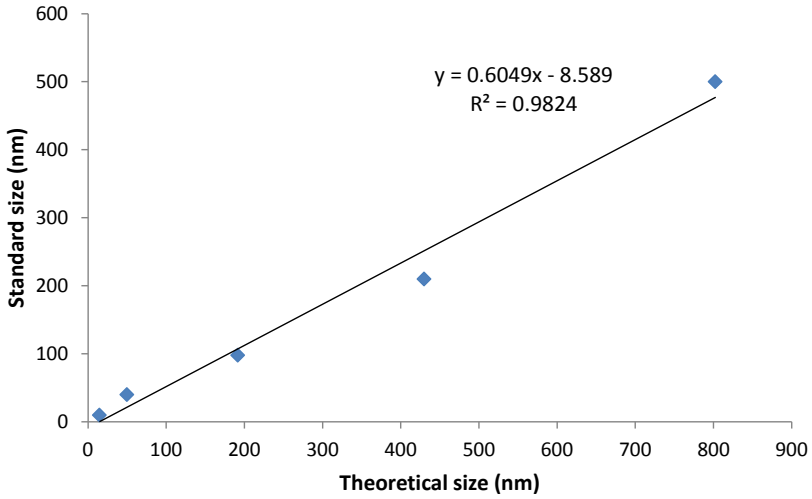

Figure A 2 Comparison between the standard size and the theoretical size

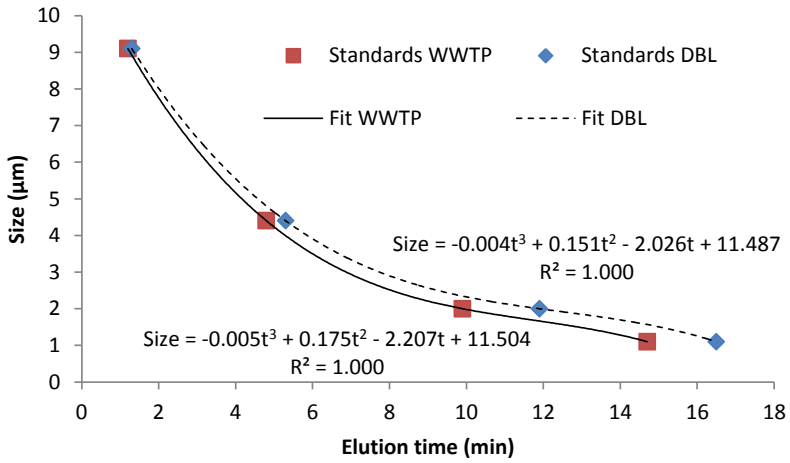

Figure A 3 Calibration equations for steric mode obtained from standard fractograms

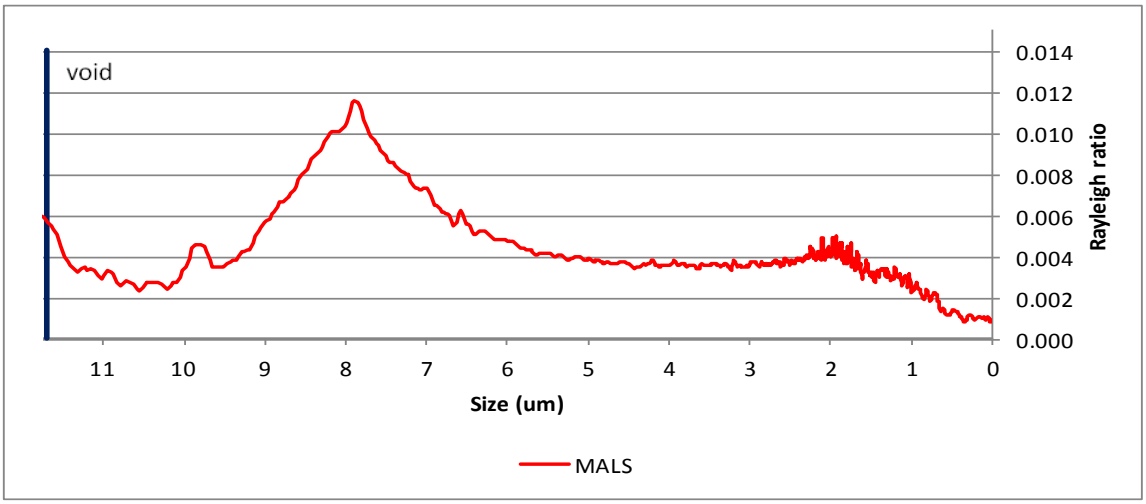

Figure A 4 WWTP sample steric mode fractogram with detection via MALS

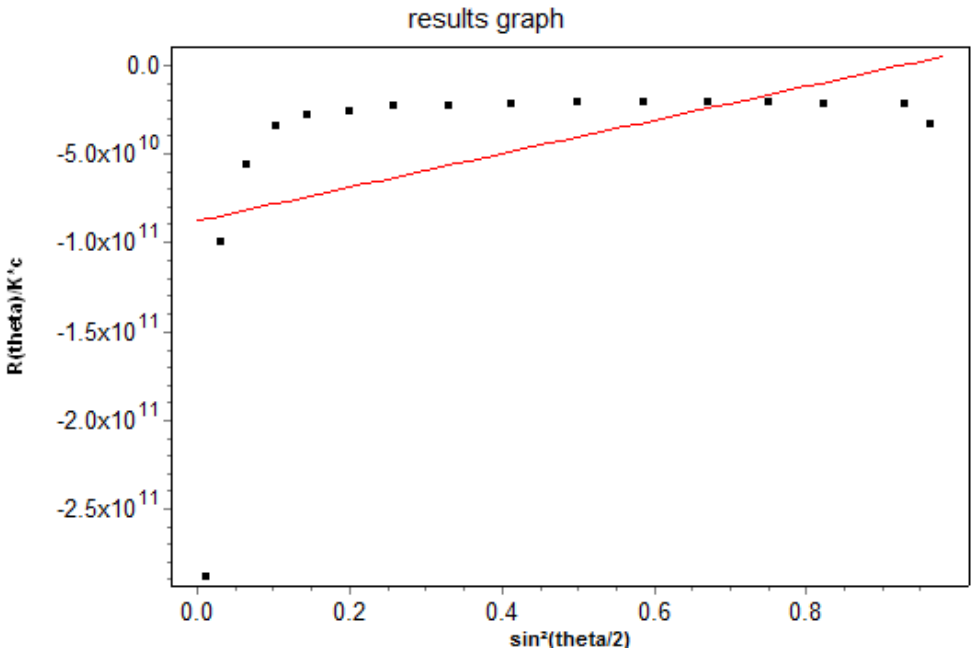

Figure A 5 Lack of angular dependence of light scattering intensity

REFERENCES

1. Diaz, X.; Johnson, W. P.; Fernandez, D.; Naftz, D. L., Size and elemental distributions of nano- to micro-particulates in the geochemically-stratified Great Salt Lake. *Applied Geochemistry* **2009,** *24*, (9), 1653-1665.

2. Baalousha, M.; Kammer, F. v. d.; Motelica-Heino, M.; Le Coustumer, P., Natural sample fractionation by FlFFF-MALLS-TEM: Sample stabilization, preparation, pre-concentration and fractionation. *Journal of Chromatography A* **2005,** *1093*, (1-2), 156-166.

3. Fabrega, J.; Luoma, S. N.; Tyler, C. R.; Galloway, T. S.; Lead, J. R., Silver nanoparticles: Behaviour and effects in the aquatic environment. *Environment International* **2011,** *37*, (2), 517-531.

4. Klaine, S. J.; Alvarez, P. J. J.; Batley, G. E.; Fernandes, T. F.; Handy, R. D.; Lyon, D. Y.; Mahendra, S.; McLaughlin, M. J.; Lead, J. R., Nanomaterials in the environment: Behavior, fate, bioavailability, and effects. *Environmental Toxicology and Chemistry* **2008,** *27*, (9), 1825-1851.

5. Zhang, T.; Kim, B.; Levard, C.; Reinsch, B. C.; Lowry, G. V.; Deshusses, M. A.; Hsu-Kim, H., Methylation of Mercury by Bacteria Exposed to Dissolved, Nanoparticulate, and Microparticulate Mercuric Sulfides. *Environmental Science & Technology* **2011,** *46*, (13), 6950-6958.

6. Richman, E. K.; Hutchison, J. E., The Nanomaterial Characterization Bottleneck. *ACS Nano* **2009,** *3*, (9), 2441-2446.

7. Harper, S. L.; Carriere, J. L.; Miller, J. M.; Hutchison, J. E.; Maddux, B. L. S.; Tanguay, R. L., Systematic evaluation of nanomaterial toxicity: Utility of standardized materials and rapid assays. *ACS Nano* **2011,** *5*, (6), 4688-4697.

8. Baalousha, M.; Stolpe, B.; Lead, J. R., Flow field-flow fractionation for the analysis and characterization of natural colloids and manufactured nanoparticles in environmental systems: A critical review. *Journal of Chromatography A* **2011,** *1218*, (27), 4078-4103.

9. Dubascoux, S.; Le Hecho, I.; Hassellov, M.; Kammer, F. v. d.; Potin Gautier, M.; Lespes, G., Field-flow fractionation and inductively coupled plasma mass spectrometer coupling: History, development and applications. *Journal of Analytical Atomic Spectrometry* **2010,** *25*, (5), 613-623.

10. Fraunhofer, W.; Winter, G., The use of asymmetrical flow field-flow fractionation in pharmaceutics and biopharmaceutics. *European Journal of Pharmaceutics and Biopharmaceutics* **2004,** *58*, (2), 369-383.

11. Kammer, F. v. d.; Legros, S.; Hofmann, T.; Larsen, E. H.; Loeschner, K., Separation and characterization of nanoparticles in complex food and environmental samples by field-flow fractionation. *TrAC Trends in Analytical Chemistry* **2011,** *30*, (3), 425-436.

12. Schimpf, M.; Caldwell, K.; Giddings, J. C., *Field flow fractionation handbook*. 2000.

13. Mitrano, D. M.; Barber, A.; Bednar, A.; Westerhoff, P.; Higgins, C. P.; Ranville, J. F., Silver nanoparticle characterization using single particle ICP-MS (SP-ICP-MS) and asymmetrical flow field flow fractionation ICP-MS (AF4-ICP-MS). *Journal of Analytical Atomic Spectrometry* **2012,** *27*, (7), 1131-1142.

14. Poda, A. R.; Bednar, A. J.; Kennedy, A. J.; Harmon, A.; Hull, M.; Mitrano, D. M.; Ranville, J. F.; Steevens, J., Characterization of silver nanoparticles using flow-field flow fractionation interfaced to inductively coupled plasma mass spectrometry. *Journal of Chromatography A* **2010,** *1218*, (27), 4219–4225.

15. Schmidt, B.; Loeschner, K.; Hadrup, N.; Mortensen, A.; Sloth, J. J.; Bender Koch, C.; Larsen, E. H., Quantitative characterization of gold nanoparticles by field-flow fractionation coupled online with light scattering detection and inductively coupled plasma mass spectrometry. *Analytical Chemistry* **2011,** *83*, (7), 2461-2468.

16. Contado, C.; Pagnoni, A., TiO2 in commercial sunscreen lotion: Flow field-flow fractionation and ICP-AES together for size analysis. *Analytical Chemistry* **2008,** *80*, (19), 7594-7608.

17. Schachermeyer, S.; Ashby, J.; Kwon, M.; Zhong, W., Impact of carrier fluid composition on recovery of nanoparticles and proteins in flow field flow fractionation. *Journal of Chromatography A* **2012,** *1264*, 72-79.

18. Leeman, M.; Islam, M. T.; Haseltine, W. G., Asymmetrical flow field-flow fractionation coupled with multi-angle light scattering and refractive index detections for characterization of ultra-high molar mass poly(acrylamide) flocculants. *Journal of Chromatography A* **2007,** *1172*, (2), 194-203.

19. Ulrich, A.; Losert, S.; Bendixen, N.; Al-Kattan, A.; Hagendorfer, H.; Nowack, B.; Adlhart, C.; Ebert, J.; Lattuada, M.; Hungerbuhler, K., Critical aspects of sample handling for direct nanoparticle analysis and analytical challenges using asymmetric field flow fractionation in a multi-detector approach. *Journal of Analytical Atomic Spectrometry* **2012,** *27*, (7), 1120-1130.

20. Hagendorfer, H.; Kaegi, R.; Traber, J.; Mertens, S. F. L.; Scherrers, R.; Ludwig, C.; Ulrich, A., Application of an asymmetric flow field flow fractionation multi-detector

approach for metallic engineered nanoparticle characterization – Prospects and limitations demonstrated on Au nanoparticles. *Analytica Chimica Acta* **2011,** *706*, (2), 367-378.

21. Chun, J.; Fagan, J. A.; Hobbie, E. K.; Bauer, B. J., Size Separation of Single-Wall Carbon Nanotubes by Flow-Field Flow Fractionation. *Analytical Chemistry* **2008,** *80*, (7), 2514-2523.

22. Gimbert, L. J.; Andrew, K. N.; Haygarth, P. M.; Worsfold, P. J., Environmental applications of flow field-flow fractionation (FIFFF). *TrAC - Trends in Analytical Chemistry* **2003,** *22*, (9), 615-633.

23. Moon, J.; Kim, S.-H.; Cho, J., Characterizations of natural organic matter as nano particle using flow field-flow fractionation. *Colloids and Surfaces A: Physicochemical and Engineering Aspects* **2006,** *287*, (1-3), 232-236.

24. Kammer, F. v. d.; Baborowski, M.; Friese, K., Field-flow fractionation coupled to multi-angle laser light scattering detectors: Applicability and analytical benefits for the analysis of environmental colloids. *Analytica Chimica Acta* **2005,** *552*, (1-2), 166-174.

25. Baalousha, M.; Lead, J. R., Size fractionation and characterization of natural aquatic colloids and nanoparticles. *Science of the Total Environment* **2007,** *386*, (1-3), 93-102.

26. Neubauer, E.; Kammer, F. v. d.; Hofmann, T., Influence of carrier solution ionic strength and injected sample load on retention and recovery of natural nanoparticles using Flow Field-Flow Fractionation. *Journal of Chromatography A* **2011,** *1218*, (38), 6763-6773.

27. Baalousha, M.; Kammer, F. v. d.; Motelica-Heino, M.; Baborowski, M.; Hofmeister, C.; Le Coustumer, P., Size-Based Speciation of Natural Colloidal Particles by Flow Field Flow Fractionation, Inductively Coupled Plasma-Mass Spectroscopy, and Transmission Electron Microscopy/X-ray Energy Dispersive Spectroscopy: Colloids-Trace Element Interaction. *Environmental Science & Technology* **2006,** *40*, (7), 2156-2162.

28. Ranville, J. F.; Chittleborough, D. J.; Shanks, F.; Morrison, R. J. S.; Harris, T.; Doss, F.; Beckett, R., Development of sedimentation field-flow fractionation-inductively coupled plasma mass-spectrometry for the characterization of environmental colloids. *Analytica Chimica Acta* **1999,** *381*, (2–3), 315-329.

29. Ebdon, L.; Collier, A. R., Direct atomic spectrometric analysis by slurry atomisation. Part 5. Analysis of kaolin using inductively coupled plasma atomic emission spectrometry. *J. Anal. At. Spectrom.* **1988,** *3*, (4), 557-561.

30. Sanz-Medel, A.; Fernandez de la Campa, M. d. R.; Gonzalez, E. B.; Fernandez-Sanchez, M. L., Organised surfactant assemblies in analytical atomic spectrometry. *Spectrochimica Acta Part B: Atomic Spectroscopy* **1999,** *54*, (2), 251-287.

31. Dubascoux, S.; Kammer, F. v. d.; Le Hecho, I.; Gautier, M. P.; Lespes, G., Optimisation of asymmetrical flow field flow fractionation for environmental nanoparticles separation. *Journal of Chromatography A* **2008,** *1206*, (2), 160-165.

32. Nischwitz, V.; Goenaga-Infante, H., Improved sample preparation and quality control for the characterisation of titanium dioxide nanoparticles in sunscreens using flow field flow fractionation on-line with inductively coupled plasma mass spectrometry. *Journal of Analytical Atomic Spectrometry* **2012,** *27*, (1), 1084-1092.

33. Kammer, F. v. d.; Baborowski, M.; Tadjiki, S.; jr., W. v. T., Colloidal Particles in Sediment Pore Waters: Particle Size Distributions and Associated Element Size Distribution in Anoxic and Re-oxidized Samples, Obtained by FFF-ICP-MS Coupling. *Acta hydrochimica et hydrobiologica* **2003,** *31*, (4-5), 400-410.

34. Baalousha, M.; Kammer, F. v. d.; Motelica-Heino, M.; Le Coustumer, P., 3D characterization of natural colloids by FlFFF-MALLS-TEM. *Analytical and Bioanalytical Chemistry* **2005,** *383*, (4), 549-556.

35. Plathe, K. L.; Kammer, F. v. d.; Hassellöv, M.; Moore, J.; Murayama, M.; Hofmann, T.; Hochella, M. F., Using FlFFF and aTEM to determine trace metal–nanoparticle associations in riverbed sediment. *Environmental Chemistry* **2010,** *7*, (1), 82-93.

36. Håkansson, A.; Magnusson, E.; Bergenståhl, B.; Nilsson, L., Hydrodynamic radius determination with asymmetrical flow field-flow fractionation using decaying cross-flows. Part I. A theoretical approach. *Journal of Chromatography A* **2012,** *1253*, (0), 120-126.

37. Nilsson, L.; Leeman, M.; Wahlund, K.-G.; Bergenståhl, B., Mechanical Degradation and Changes in Conformation of Hydrophobically Modified Starch. *Biomacromolecules* **2006,** *7*, (9), 2671-2679.

38. Moon, M. H.; Williams, P. S.; Kwon, H., Retention and Efficiency in Frit-Inlet Asymmetrical Flow Field-Flow Fractionation. *Analytical Chemistry* **1999,** *71*, (14), 2657-2666.

39. Litzen, A.; Wahlund, K. G., Zone broadening and dilution in rectangular and trapezoidal asymmetrical flow field-flow fractionation channels. *Analytical Chemistry* **1991,** *63*, (10), 1001-1007.

40. Giddings, J. C., Simplified nonequilibrium theory of secondary relaxation effects in programmed field-flow fractionation. *Analytical Chemistry* **1986,** *58*, (4), 735-740.

41. Wahlund, K.-G., Flow field-flow fractionation: Critical overview. *Journal of Chromatography A* **2013,** *1287*, (0), 97-112.

42. Hee Moon, M.; Williams, P. S.; Kang, D.; Hwang, I., Field and flow programming in frit-inlet asymmetrical flow field-flow fractionation. *Journal of Chromatography A* **2002,** *955*, (2), 263-272.

43. Kirkland, J. J.; Dilks Jr, C. H.; Rementer, S. W.; Yau, W. W., Asymmetric-channel flow field-flow fractionation with exponential force-field programming. *Journal of Chromatography A* **1992,** *593*, (1–2), 339-355.

44. Magnusson, E.; Håkansson, A.; Janiak, J.; Bergenståhl, B.; Nilsson, L., Hydrodynamic radius determination with asymmetrical flow field-flow fractionation using decaying cross-flows. Part II. Experimental evaluation. *Journal of Chromatography A* **2012,** *1253*, (0), 127-133.

45. Hansen, M. E.; Giddings, J. C.; Schure, M. R.; Beckett, R., Corrections for secondary relaxation in exponentially programmed field-flow fractionation. *Analytical Chemistry* **1988,** *60*, (14), 1434-1442.

46. Ruiz, A. I.; Canals, A.; Hernandis, V., Effect of surfactants in flame atomic absorption spectrometry with pneumatic nebulization: influence of hydrophobic chain length. *Journal of Analytical Atomic Spectrometry* **1993,** *8*, (1), 109-113.